Available online at www.sciencedirect.com
ScienceDirect
International Journal of Multiphase Flow 34 (2008) 227–240
International Journal of Multiphase Flow
www.elsevier.com/locate/ijmulflow

Theoretical analysis of capillary-driven nanoparticulate slurry flow during a micromold filling process

A. Mawardi, Y. Xiao, R. Pitchumani *

Advanced Materials and Technologies Laboratory, Department of Mechanical Engineering, University of Connecticut, Storrs, CT 06269-3139, United States

Received 18 September 2006; received in revised form 21 June 2007

Abstract

The microcasting technique for the fabrication of microstructures mainly involves two consecutive steps, namely, the capillary-driven flow of nanoparticulate slurry in micromolds and sintering of the resulting preform. During the mold-filling step, particle settling leads to a spatial particle distribution in the preform, which affects the subsequent sintering kinetics, and in turn, and causes a shape distortion in the final sintered product. This paper presents a comprehensive theoretical model which is adopted to account for the capillary-driven flow and simultaneous particle settling behavior during the filling step. Numerical simulations are performed over a wide range of parameters to illustrate the effects of four nondimensional groups on the fill time and particle distribution, and to develop design windows, which may serve as guidelines in the design of particle properties, slurry composition, and mold dimensions to maintain a desired level of homogeneity in particle distribution.

Keywords: Particulate slurry; Microchannel; Particle distribution; Capillary flow; Particle settling

1. Introduction

Fabrication of microstructures has emerged as an important issue in modern technologies, and techniques such as LIGA (a German acronym for lithography, electrodeposition, and molding) and silicon surface micromachining, have been developed to produce the microstructures that are widely used in microelectronics, micro optical devices, and microfluidic systems (Piotter et al., 2002; Hormes et al., 2003). However, these fabrication techniques are suited to only a limited set of materials such as electroformable metals or polymers (Garino et al., 2002, 2004; Morales et al., 2005), and the wear resistance and strength of the parts are generally low (Gietzelt et al., 2002). A novel technique based on microcasting has been developed for the fabrication of microparts with high aspect ratio and straight side walls from a broader material suite of metals, alloys, and ceramics, improving the micropart properties (Morales et al., 2001, 2002, 2005; Garino et al., 2002, 2003, 2004; Allan et al., 2003; Merz et al., 2004).

The steps involved in the microcasting process are illustrated schematically in Fig. 1, and consist of the following: capillary-driven flow of a slurry composed of catalyzed epoxy resin and solid nanoparticles of metal or ceramic into a sacrificial micromold made of polymethylmethacrylate (PMMA); curing of the slurry in the mold to yield a nanoparticulate composite with sufficient structural integrity to be demolded, planarized, and handled without damage; exposing the preform to a high temperature cycle to burn off the organic phase and to sinter the porous nanoparticulate green body to a monolithic final micropart. During the filling process, depending upon the slurry composition and design, sedimentation or floating (referred to, generally, as settling in this paper) of the nanoparticles may occur causing inhomogeneous nanoparticulate distribution and, in turn, nonuniform porosity in the green preform. Sintering of the preform with inhomogeneous

* Corresponding author. Tel.: +1 860 486 0683; fax: +1 860 486 5088.
E-mail address: pitchu@engr.uconn.edu (R. Pitchumani).

0301-9322/$ - see front matter © 2007 Elsevier Ltd. All rights reserved.
doi:10.1016/j.ijmultiphaseflow.2007.07.004

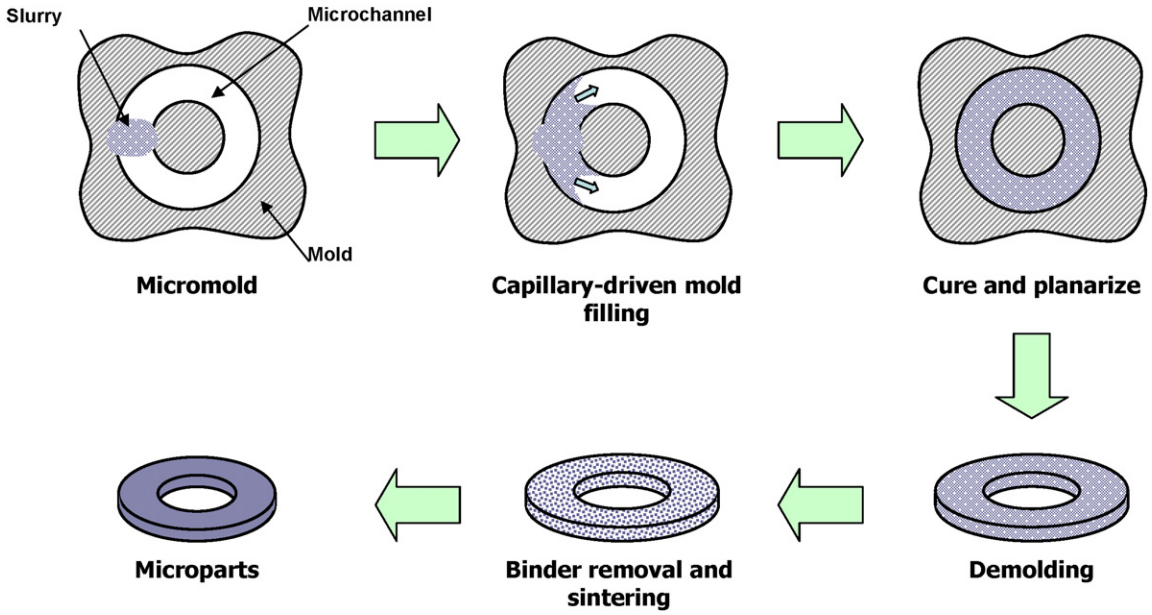

Fig. 1. Schematic of the steps involved in the microcasting process (redrawn from Morales et al., 2005).

porosity distribution will result in micropart shape distortions, which are sought to be minimized or eliminated. An analysis of the capillary-driven flow and nanoparticulate settling during flow is imperative for an effective design of the slurry, the micromold, and the microcasting process so as to achieve uniform particulate distribution in the preform prior to sintering. This forms the motivation for the present study.

Capillary flow in channels and settling phenomenon of particles in a dispersed two-phase flow have each been studied quite extensively in the literature. The classical Washburn equation (Washburn, 1921) based on a balance of viscous force, surface tension and gravity governs the long-term capillary rise behavior. Theoretical analyses extending the Washburn description to include entrance effects and dynamic contact angle variation have also been since reported (Levine et al., 1976; Dreyer et al., 1993, 1994; Hamraoui et al., 2000, Hamraoui and Nylander, 2002; Xiao et al., 2006). Horizontal capillary-driven flow has relatively been less studied than flow in vertical capillaries: Brittin (1946) obtained an approximate solution based on the assumptions of small capillary radius and negligible end-effects. Recently, Morales et al. (2005) investigated flow of ceramic and metallic nanoparticulate slurries in rectangular open channel micromolds by employing the integral method, but did not consider the settling behavior of the particles during flow.

Research on the settling phenomenon in a dispersed two-phase flow traces its origins to the pioneering work by Kynch (1952) who developed a sedimentation theory based on the assumption that the settling velocity of a particle is a function of local particle concentration. Later, this theory has been extended and applied in many fields, such as the settling of slurries in batch and continuous thickeners (Shannon and Tory, 1965), and the sedimentation of monodisperse, possibly flocculated, and polydisperse flocculated suspension (Bürger and Concha, 1998, Bürger et al., 2001). The studies have demonstrated that the kinematic sedimentation theory is effective in describing the particle settling phenomenon. However, to the authors' knowledge, particle settling during capillary-driven flow in a horizontal open microchannel, as encountered in the microcasting process, has not been studied.

With the goal of understanding the governing physical phenomena during the mold-filling process, and determining the range of parameters to maintain a desired level of homogeneity in the particle distribution, a theoretical model for the slurry flow in a rectangular, open cavity microchannel is developed in this paper. The capillary-driven flow of the slurry is described by means of an integral analysis, and the settling of the solid particles is modeled using kinematic sedimentation theory to consider cases of sinking as well as floating of particles in the slurry. The particle concentration distribution alters the slurry viscosity distribution and, in turn, affects the flow progression. The instantaneous particle distribution is determined by the flow velocity, which results in a two-way coupling between the flow and particle settling. Based on the theoretical model, a systematic study is conducted to predict the particle distribution and the time-dependent flow progression into the channel, as a function of four nondimensional groups representing different flow and settling parameters. The results of the parametric studies are then developed into design windows to determine the range of nondimensional groups for a desired uniform porosity distribution, which may provide useful guidelines for the development of the mold-filling step, and further, aid the simulation and design of the sintering step of the microcasting process.

The paper is organized as follows: the detailed formulation of the governing equations and the numerical solution procedures are presented in Section 2, followed by a discussion of the parametric study results and the design windows for various parameter combinations in Section 3.

2. Theoretical model

A schematic illustration of mold filling in a rectangular micromold during the microcasting process is presented in Fig. 2. Driven by capillary effect, the particulate slurry in the reservoir flows into a rectangular, open cavity microchannel of width W, and height H, and forms a three-dimensional meniscus at the flow front. As shown in Fig. 2, the axes x, y, and z correspond to the direction of the flow, across the channel, and the direction along the height, respectively. The filling is considered to be isothermal as in the processing experiments by Morales et al. (2005). The slurry is treated as an incompressible, Newtonian fluid with an initially homogeneous particle distribution. The theoretical model is developed following a formulation similar to that employed in the work of Morales et al. (2005), with the major distinction that particle settling effects are considered and coupled to the flow. The goal of the modeling is to determine the time-evolution of the flow front progression and the spatial nanoparticulate distribution in the flowing slurry.

The governing equation for the time-dependent fill length is derived based on an integral formulation of the conservation of mass and linear momentum. By considering a deformable control volume encompassing the filled region in the channel, denoted by the dashed line in Fig. 2, the integral momentum equation along the x-direction may be written as:

$$\sum F_x = \frac{\mathrm{d}}{\mathrm{d}t}\left[\int_0^H \int_{-\frac{W}{2}}^{\frac{W}{2}} \int_0^{L_\mathrm{f}} \rho v_x \,\mathrm{d}x\,\mathrm{d}y\,\mathrm{d}z\right] + \int_0^H \int_{-\frac{W}{2}}^{\frac{W}{2}} v_x(-\rho v_x)\,\mathrm{d}y\,\mathrm{d}z \tag{1}$$

Note that instead of the actual height of the free surface, the channel height H, is used as the upper limit of the integral, which means that the slurry is assumed to fill the whole channel height across the width of the channel, and the meniscus shape along the channel width is neglected. This assumption is generally valid except for cases that $W \ll H$ (Morales et al., 2005). The fill length L_f, is sought to be determined, as a function of time t, and the other terms in Eq. (1) are as follows: ρ is the slurry density, and v_x is the x-component of slurry velocity; F_x represents all the forces acting on the deformable control volume in the x-direction, which includes the pressure forces at the inlet to the channel and at the flow front, i.e., F_pi and F_pf, and the viscous force F_v. The terms on the right-hand side of Eq. (1) are identified as the rate of momentum change in the control volume, and the momentum flux through the control surface. The inlet pressure force F_pi, can be written as:

$$F_\mathrm{pi} = \int_0^H \int_{-\frac{W}{2}}^{\frac{W}{2}} p(0,y,z,t)\,\mathrm{d}y\,\mathrm{d}z \tag{2}$$

where $p(0,y,z,t)$ is the inlet pressure, which will be discussed later in this section. The pressure force at the flow front arises from the surface tension at the interface between the slurry and the surrounding air, which provides a driving force for the capillary flow. This force can be expressed as:

$$F_\mathrm{pf} = \left[p_\infty - \sigma\cos\theta_\mathrm{d}\left(\frac{2}{W}+\frac{1}{H}\right)\right]WH \tag{3}$$

where p_∞ is the ambient pressure, σ is the surface tension of the slurry in contact with air, and θ_d is the dynamic contact angle between the advancing slurry meniscus and the microchannel surfaces. As indicated in many studies, the penetration rate strongly depends on the dynamic contact angle (Berezkin and Churaev, 1982), and, therefore, instead of the constant static contact angle θ_e, the dynamic contact angle is used in this paper. For the spontaneous penetration process, the dynamic contact angle θ_d starts with an initial value close to 90° and gradually evolves to the equilibrium value θ_e (Schonhorn et al., 1966; Newman, 1968; Summ and Raud, 1991; Han and Wang, 1997; Soboleva et al., 2000). The relaxational spreading model developed

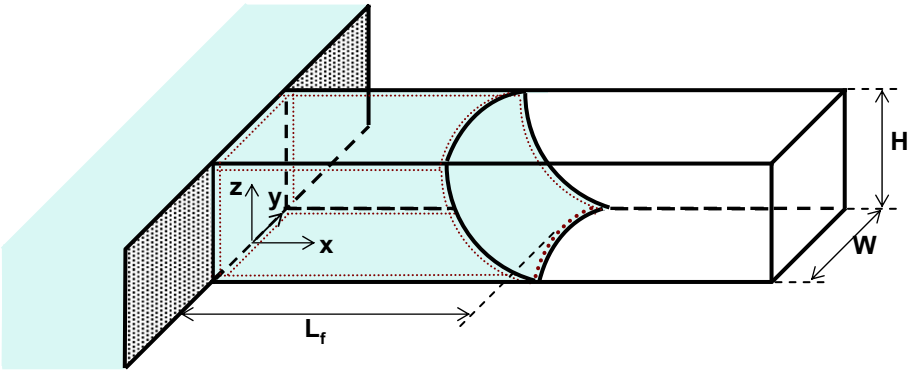

Fig. 2. Schematic of the model domain identifying the geometric parameters and the coordinate system used in the theoretical development. The dashed lines denote the control volume used in the model formulation.

by Newman (1968) and later researchers (Summ and Raud, 1991; Han and Wang, 1997; Soboleva et al., 2000) is employed here to describe the time-evolution of the contact angle during the filling process (Morales et al., 2005):

$$\cos\theta_d = \cos\theta_e[1 - \exp(-\sigma t/\eta_0 M)] \tag{4}$$

where η_0 is the viscosity of the homogeneously dispersed nanoparticulate slurry in the reservoir. Although the dynamic contact angle may depend on the local slurry viscosity at the contact line, to simplify the formulation, the viscosity corresponding to the initial homogeneous slurry in the reservoir is used in the simulation. Its validity is verified in a later section on presentation of the results. The parameter M in Eq. (4) is interpreted as a characteristic length over which the relaxational spreading takes place. The value of M varies with the specific combination of the fluid and contact surface properties.

To evaluate the viscous force and last two terms in Eq. (1), the distribution of velocity field is required. Since the spontaneous capillary flow is laminar in nature with the Reynolds number on the order of 10 (Duarte et al., 1996; Barraza et al., 2002), the flow is assumed to be fully developed with a double parabolic profile as follows:

$$v_x(y,z,t) = C_0(t)\left[\left(\frac{W}{2}\right)^2 - y^2\right](2Hz - z^2)$$

where $C_0(t)$ is a time-dependent function, which can be determined by equating the average velocity for a channel cross-section to the progression rate of the flow front $\frac{dL_f}{dt}$, i.e., $C_0(t) = \frac{9}{(WH)^2}\frac{dL_f}{dt}$. The assumption of fully developed flow means that any deviation from the parabolic velocity profile in the entrance region and at the flow front are neglected. Therefore, the x-component of velocity v_x is given by:

$$v_x(y,z,t) = 9\frac{dL_f}{dt}\left[\frac{1}{4} - \left(\frac{y}{W}\right)^2\right]\frac{z}{H}\left(2 - \frac{z}{H}\right) \tag{5}$$

The above expression automatically satisfies the no-slip boundary conditions at the bottom ($z = 0$) and size walls ($y = \pm\frac{W}{2}$) of the channel, and zero-shear stress at the top free surface ($z = H$). Applying this double parabolic velocity profile, the viscous force along the bottom wall and side walls is evaluated as

$$F_v = 2\int_0^{L_f}\int_0^{H}\left[-\eta(\phi)\frac{\partial v_x}{\partial y}\right]_{y=\pm\frac{W}{2}} dx\,dz + \int_0^{L_f}\int_{-\frac{W}{2}}^{\frac{W}{2}}\left[\eta(\phi)\frac{\partial v_x}{\partial z}\right]_{z=0} dx\,dy \tag{6}$$

where $\eta(\phi)$ is the local slurry viscosity, which is a function of ϕ, the particle volumetric concentration. Similarly, the last two terms in Eq. (1) are obtained as:

$$\frac{d}{dt}\left[\int_0^H\int_{-\frac{W}{2}}^{\frac{W}{2}}\int_0^{L_f}\rho v_x\,dx\,dy\,dz\right] = \rho_0 WH\left[L_f\frac{d^2L_f}{dt^2} + \left(\frac{dL_f}{dt}\right)^2\right] \tag{7}$$

$$\int_0^H\int_{-\frac{W}{2}}^{\frac{W}{2}} v_x(-\rho v_x)\,dy\,dz = -\frac{36}{25}\rho_0 WH\left(\frac{dL_f}{dt}\right)^2 \tag{8}$$

The inlet pressure $p(0,y,z,t)$ is estimated through an integral analysis of the flow in a hemispherical control volume abutting the entrance within the reservoir (Morales et al., 2005), such that the diameter of the hemisphere is determined by equating the projected area on the y–z plane to that of the channel inlet. The velocity distribution outside the hemispherical control volume is assumed to be that of a sink flow. Following similar approaches in the literature (Levine et al., 1976; Dreyer et al., 1993, 1994), the inlet pressure takes the form:

$$p(0,y,z,t) = p_\infty - \rho_0\left[0.6\sqrt{WH}\frac{d^2L_f}{dt^2} + \frac{3.545}{\sqrt{WH}}\left(\frac{\eta_0}{\rho_0}\right)\frac{dL_f}{dt} + 1.398\left(\frac{dL_f}{dt}\right)^2\right] \tag{9}$$

where ρ_0 is the density of the homogeneously dispersed nanoparticulate slurry in the reservoir. Note that the constants in Eq. (9) are derived from the analysis.

Substituting Eq. (9) into Eq. (2), and Eq. (4) into Eq. (3) yields the pressure forces F_{pi} and F_{pf}. Evaluating all the terms in Eq. (1) by employing Eqs. (2), (3), and Eqs. (6)–(8), the resulting integro-differential governing equation for the time-dependent fill length L_f is obtained as:

$$\left(L_f + 0.6\sqrt{WH}\right)\frac{d^2L_f}{dt^2} + 0.958\left(\frac{dL_f}{dt}\right)^2 + \left[\frac{18}{\rho_0 W^2 H}\int_0^{L_f}\int_0^H\left[\eta(\phi)\left(\frac{2z}{H} - \frac{z^2}{H^2}\right)\right]_{y=\pm\frac{W}{2}} dx\,dz + \frac{3}{\rho_0 H^2}\int_0^{L_f}[\eta(\phi)]_{z=0}\,dx + \frac{3.545\eta_0}{\rho_0\sqrt{WH}}\right]\frac{dL_f}{dt} = \frac{\sigma}{\rho_0}\cos\theta_e(1 - e^{-\sigma t/\eta_0 M})\left(\frac{1}{H} + \frac{2}{W}\right) \tag{10}$$

The determination of the fill length L_f using Eq. (10) requires the viscosity information, $\eta(\phi)$, as a function of particle distribution ϕ, which may be solved by considering the particle settling during the flow. For simplicity, the slurry is assumed to be an ideal suspension with spherical particles, whose settling velocity only depends on the local particle volumetric concentration. There is no mass transfer between the solid and the liquid phases. Further, the variation of particle distribution across the channel width, i.e., the dependence of ϕ on the y-position, is neglected, and for the present analysis, the effect of dispersants, surfactants, interparticle forces, and Brownian motions are ignored. In terms of a Lagrangian view, the mass conservation for the particulates is given by:

$$\frac{\partial \phi}{\partial t} + \frac{\partial(\phi v_s)}{\partial z} = 0 \tag{11}$$

where v_s is the solid phase velocity, which is also a function of particle concentration ϕ. In order to describe the settling behavior of the particulates even when the solid concentration approaches the maximum value ϕ_{max}, the modified Batchelor's equation (Batchelor, 1982) proposed by Bürger et al. (2001) is used for the solid phase velocity:

$$v_s = v_t\left(1 - \frac{\phi}{\phi_{max}}\right)^2 \exp\left[\phi\left(S_{11} + \frac{2}{\phi_{max}}\right)\right] \tag{12}$$

where ϕ_{max} is the maximum value of solid volume fraction due to the spaces left between the spherical particles, which is taken to be 0.68 in this study (Concha et al., 1992), and the coefficient, S_{11}, is approximated using the results from Batchelor and Wen (1982) assuming the case of single particle species. The Stokes velocity v_t is defined as the settling velocity of a single spherical particle in a pure fluid:

$$v_t = -\frac{2(\rho_s - \rho_l)gr^2}{9\eta_l} \tag{13}$$

where ρ_s, ρ_l are the densities of the solid and liquid epoxy phase, respectively, g is the gravitational acceleration, r denotes the radius of a single spherical nanoparticle, and η_l is the dynamic viscosity for the epoxy liquid. Recall that the term settling as used in this paper refers to the particle migration to the channel bottom (particle sinking) as well as rise of the particles to the top of the fluid (floating) depending on whether $v_t < 0$ or $v_t > 0$, respectively.

Since the solid particles can not penetrate through the bottom wall and the free surface at the top, the boundary conditions corresponding to the governing equation, Eq. (11), are zero flux at these two boundaries, which may be written as:

$$(v_s\phi)_{z=0} = 0; \quad (v_s\phi)_{z=H} = 0 \tag{14}$$

It should be pointed out that Eq. (11) is a first-order partial differential equation for the particle volume fraction ϕ, but due to the discontinuous changes in the particle concentration across the height of the channel, two boundary conditions are used to give two different solutions that are connected by a solution in the interior posing a shock layer. The coupled governing equations (Eqs. (10) and (11)) are subject to the following initial conditions: (1) zero fill length and penetration rate; (2) homogeneous particle distribution, mathematically expressed as:

$$L_f(0) = \frac{dL_f}{dt}(0) = 0; \quad \phi(0,z) = \phi_0 \tag{15}$$

Eq. (10), a nonlinear, second-order ordinary integro-differential equation, coupled with Eq. (11), a first-order partial differential equation, constitutes a governing equation group to determine the fill length as a function of time, which is solved numerically using a fifth-order Runge–Kutta scheme with adaptive step size (Press et al., 1986). For each time step specified by the Runge–Kutta algorithm, Eq. (11) is solved by means of a nonstaggered second-order central difference scheme proposed by Kurganov and Tadmor (2000), which is a high-resolution, shock-capturing scheme. Once the solid phase volume fraction distribution is obtained for each time step, the empirical expression for slurry rheology reported by Morales et al. (2005):

$$\eta = 0.223(1 - \phi)^{-6.525} \tag{16}$$

is employed to evaluate the local slurry viscosity as a function of particle volume fraction, $\eta(\phi)$, used in Eq. (10). The above relationship between the slurry viscosity and particle volume fraction follows a Krieger–Dougherty form (Krieger and Dougherty, 1959), and may be replaced by a different form, depending on the characteristics of the slurry, but the same numerical procedure applies without loss of generality. The viscosity $\eta(\phi)$ in the integrands in Eq. (10), requires the distribution of the particle volume fraction in two spatial directions x and z, as $\phi(x,z)$, whereas the solution of Eq. (11) yields the volume fraction as a function of time t, and space in z-direction, $\phi(t,z)$. The transformation from $\phi(t,z)$ to $\phi(x,z)$ is possible by considering t in Eq. (11) as Lagrangian time which relates to the flow front velocity $\frac{dL_f}{dt}(t)$, as a function of time, as:

$$x(t) = \int_0^t \frac{dL_f}{dt}(\tau)\,d\tau \tag{17}$$

where τ is the integration variable representing the time.

The solution of the system of equations and associated conditions given by Eqs. (10), (11), and (15), yields the transient fill length $L_f(t)$, as a function of the microchannel dimensions, and slurry properties (which, in turn, incorporate the particle loading in the slurry). The solid phase volume fraction $\phi(x,z)$ obtained from the analysis may be used as initial porosity distribution for the porous part at the beginning of sintering process. The next section describes the results obtained from the simulations using the theoretical model.

3. Results and discussion

The theoretical model was validated by comparing the predictions of time-evolution of fill length $L_f(t)$, through a rectangular microchannel of width 515 μm and height 170 μm, with the experimental data reported by Morales et al. (2005). The results of the validation are presented in Fig. 3, where the solid line corresponds to the present simulation results, while the discrete markers denote the experimental data. Two nanoparticulate alumina/epoxy slurry compositions are considered for the validation: one with 71% by volume epoxy slurry (Fig. 3a), and the other with 53% by volume epoxy slurry (Fig. 3b). The figures show that the results of the theoretical model are in good agreement with the experimental data for both cases presented. It should be noted that the numerical results are also close to the theoretical predictions obtained by Morales et al. (2005), where the particle

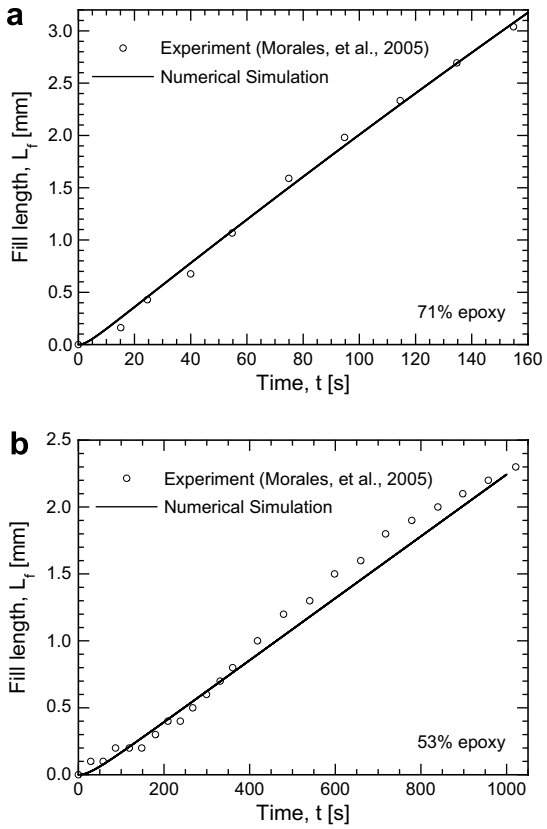

Fig. 3. Comparison of the simulation using the current model with experimental data from Morales et al. (2005).

settling phenomenon is ignored, suggesting that settling may not be significant for the particular combination of parameters in the slurry formulation used. However, depending on the choice of slurry and mold parameters, settling of particles could be important. The results presented in this section are aimed at delineating such regimes of parameters.

Based on the foregoing validation, the theoretical model is nondimensionalized to allow for more general physical interpretation of the results. Since the particle settling along the z-direction is the focus of the investigation, the height of the channel H is chosen as the characteristic length, and a characteristic time is defined as $t_0 = \frac{\rho_0 H^2}{\eta_0}$. The dimensionless governing equations and boundary conditions may be obtained from Eqs. (10), (11), (14), and (15), and are omitted here for brevity. Four nondimensional groups are identified as follows: (1) the initial homogeneous volume fraction of the slurry as it enters the channel, ϕ_0; (2) normalized Stokes velocity, U_t^*, defined as the ratio of the Stokes velocity to a characteristic velocity of flow, $U_t^* = -\frac{2(\rho_s-\rho_l)gr^2}{9\eta_l}\frac{\rho_0 H}{\eta_0}$; (3) the Ohnesorge number representing the ratio of viscous force to the surface tension, $Oh = \frac{\eta_0}{\sqrt{\sigma\rho_0 H}}$, and (4) the aspect ratio $\gamma = \frac{H}{W}$ of the rectangular channel. For the parametric simulations, the values of the nondimensional groups are chosen to represent a wide range of microcasting dimensions, flow parameters, and compositions of the slurries. Note that for the epoxy–alumina nanoparticulate slurry flow reported by Morales et al. (2005) and used in the above validation, the corresponding nondimensional parameters are: $U_t^* = 7.37\times 10^{-8}$, $Oh = 31.28$, and $\gamma = 0.33$. In the present study, the simulations were conducted for the nondimensional channel length of $L^* = \frac{L}{H} = 20.6$. Two types of settling of nanoparticles are considered in this study: (1) the case where the density of particulates ρ_s is larger than the density of fluid, ρ_l, such that $\rho_s/\rho_l = 3.6$, constituting the case of particles sedimentation to the bottom, and (2) where ρ_s is smaller than ρ_l, such that $\rho_s/\rho_l = 1.0/3.6$, for which the resulting Stokes velocity is positive, $v_t > 0$, as per Eq. (13), and the solid particles float to the top of the fluid. Thus, the term settling as used in this section refers to both the sinking and floating of the nanoparticles.

Fig. 4 presents the effects of the magnitude and sign of the normalized Stokes velocity on the fill length and particle distribution for different values of normalized Stokes velocity: 1×10^{-8}, 5×10^{-9}, and 1×10^{-10}, representing the floating case, and -1×10^{-10}, -5×10^{-9}, and -1×10^{-8}, representing the sinking case. The results correspond to an initial particle volume fraction of $\phi_0 = 0.30$, Ohnesorge number of $Oh = 20$, and a microchannel aspect ratio of $\gamma = 0.33$. The increase in the magnitude of the normalized Stokes velocity signifies the increase of the settling rate relative to the characteristic flow rate. Fig. 4a shows the time-evolution of the dimensionless fill length $L_f^* = L_f/H$, where it is seen that for a given initial particle volume fraction, the time to reach a given fill length varies monotonically with respect to the normalized Stokes velocity. The solid line in Fig. 4a corresponds to the results for zero normalized Stokes velocity, denoting the absence of settling phenomenon, where neither sinking nor floating of particles occurs. As the normalized Stokes velocity decreases from $U_t^* = 1\times10^{-8}$ to 5×10^{-9}, there is less settling of particles toward the top of the channel, which increases the flow resistance in the bottom of the channel, in turn, reducing the flow rate and increasing the fill time. As the normalized Stokes velocity decreases further to 1×10^{-10}, the fill time asymptotically approaches the results of the nonsettling case. As the normalized Stokes velocity reverses in sign, and the magnitude increases up to -1×10^{-8}, the fill time is seen to monotonically increases. Physically, as the rate of particles settling in the bottom of the channel increases during the flow, the overall flow resistance increases resulting in an increasing fill time with the magnitude of the normalized Stokes velocity.

The particle settling behavior is further evident in the contours of particle volume fraction distribution in Fig. 4b–f, which illustrate the solid particle distribution in the slurry at the end of the filling process. Note that since the particulate variation along the channel width (y-direction) is considered to be uniform in the analysis, the solid fraction profile is presented along the dimensionless x^*–z^* plane ($x^* = x/H$; $z^* = z/H$), for three different normalized Stokes velocities representing the sinking cases (Fig. 4b,d,

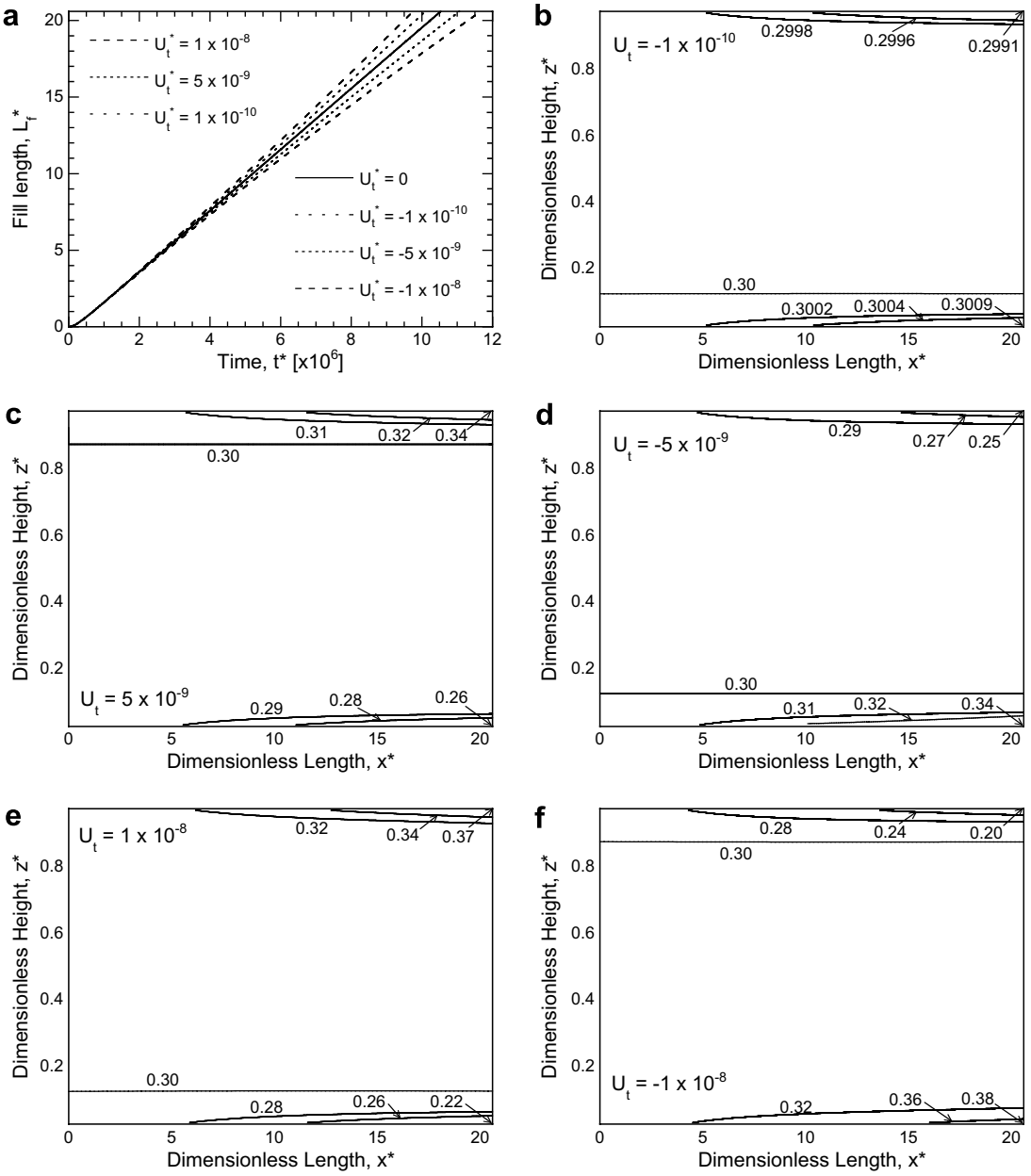

Fig. 4. (a) Effects of normalized Stokes velocity U_t^* on the fill time of slurry flow; and the corresponding particulate volume fraction distributions for the normalized Stokes velocity of (b) -1×10^{-10}, (c) 5×10^{-9}, (d) -5×10^{-9}, (e) 1×10^{-8}, and (f) -1×10^{-8}.

and f), and two representing the floating cases (Fig. 4c and e). Fig. 4b, d and f show that the particle volume fraction ϕ at the bottom of the channel increases, while the ϕ at the top of the channel decreases along the length of the channel (along x^*-direction), indicating the sedimentation of the nanoparticulates during the filling process, while Fig. 4c and e present the reverse trend for the floating cases. The plots also show that an initially homogeneous particulate distribution at the channel entrance ($x^* = 0$) results in increasing inhomogeneity toward the end of the channel ($x^* = 20.6$). Fig. 4b–f also indicate that a large middle portion of the channel height maintains the uniform initial particle concentration ϕ_0 of 0.3, and that this region of $\phi = 0.3$ contracts along the channel length as the slurry flows into the channel.

For a small value of the normalized Stokes velocity of $U_t^* = -1 \times 10^{-10}$ (a sinking case, Fig. 4b), the particles do not exhibit significant settling during the flow through the channel; however, as the magnitude of normalized Stokes velocity increases to $U_t^* = -5 \times 10^{-9}$ (Fig. 4d), the particles begin to accumulate at the bottom of the channel, reducing the concentration at the top of the channel. The corresponding increase in the viscosity at the bottom of the channel decreases the flow velocity, while the decrease in the viscosity at the top of channel is not large enough to significantly increase the flow, and the net result is the

decrease of the average flow velocity. The particle distribution corresponding to a normalized Stokes velocity of 5×10^{-9}, which denotes the case of floating of nanoparticles, is shown in Fig. 4c, where it is seen that the particle distribution is reversed relative to that in Fig. 4d, with similar contour lines and values. The reduced concentration in the bottom of the channel decreases the flow resistance, allowing for faster fill time, as seen in Fig. 4a. As the magnitude of normalized Stokes velocity increases further to 1×10^{-8}, for the floating case (Fig. 4e), an increase of concentration of solid particles is seen at the top of the channel, and further decreases the concentration in the bottom of the channel. A similar but directionally reversed solid particle distribution is seen in Fig. 4f corresponding to the results for the sinking case with the same magnitude of normalized Stokes velocity. From these large magnitude of U_t^* cases, a significant increase in settling of the solid particles in the bottom of the flow channel significantly increases the overall flow resistance and the fill time.

The effects of initial slurry concentration on the flow characteristics and the particulate settling behavior is presented in Fig. 5 by considering three different initial particle volume fractions of $\phi_0 = 0.10$, 0.30, and 0.50 for a sinking case ($\rho_s/\rho_l = 3.6$) corresponding to the normalized Stokes velocity, $U_t^* = -5 \times 10^{-9}$, Ohnesorge number, $Oh = 20$, and aspect ratio, $\gamma = 0.33$. It is seen in Fig. 5a that the time to fill any given microchannel length increases as the initial particle volume fraction increases, as physically expected. For the initial particle volume fraction $\phi_0 = 0.10$, the dimensionless fill time for the slurry to fill the complete length of the channel is 7.2×10^6, while this value increases to 11.1×10^6 for a slurry with $\phi_0 = 0.30$, and 13.5×10^6 for $\phi_0 = 0.50$. The increase in the fill time is due to the increased viscosity associated with the larger initial particulate fraction in the slurry, as per Eq. (16). The inhomogeneity is greater for the larger particulate loading as noted in the trend in the profiles from Fig. 5b–d. This is attributed to the fact that as the particle loading increases, the slurry viscosity increases, leading to longer fill times, and, in turn, providing more time for the settling to occur.

Noticeably similar results are shown in Fig. 6 which shows the effects of initial slurry concentration on the flow and settling characteristics for the floating case where $\rho_s/\rho_l = 1.0/3.6$. Fig. 6a shows that the fill time increases with initial particle volume fraction with similar increase in magnitude shown in Fig. 5a. Fig. 6b–d also show that the particle distributions are similar to the results shown in Fig. 5b–d inverted with respect to the mid-channel height. The slight difference in fill time and the maximum and minimum particle concentrations is due to the fact that the flow with floating particles is slightly faster than that with sinking particles, following the discussion of Fig. 4. Recognizing the quantitative and qualitative similarity of the results for sinking and floating cases, the following dis-

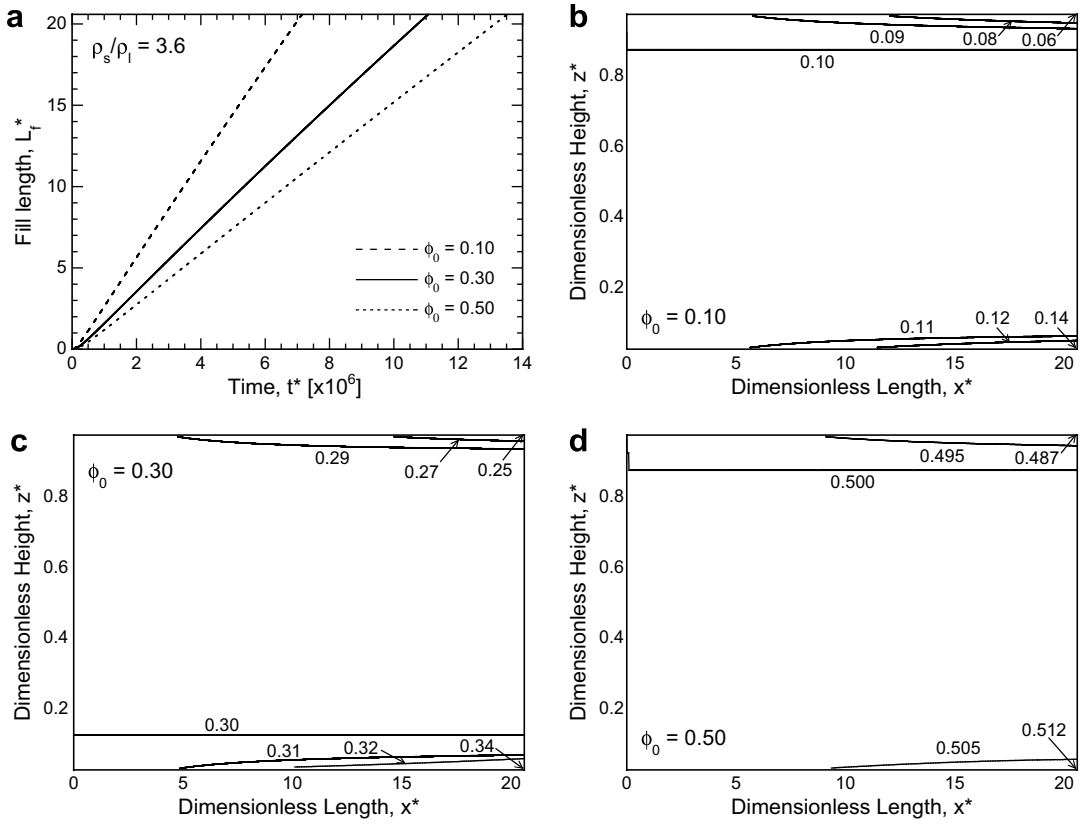

Fig. 5. (a) Effects of initial particle volume fraction ϕ_0 on the fill time; and the corresponding particulate volume fraction distributions for the initial volume fraction of (b) 0.10, (c) 0.29, and (d) 0.47, for sinking case where $\rho_s/\rho_l = 3.6$.

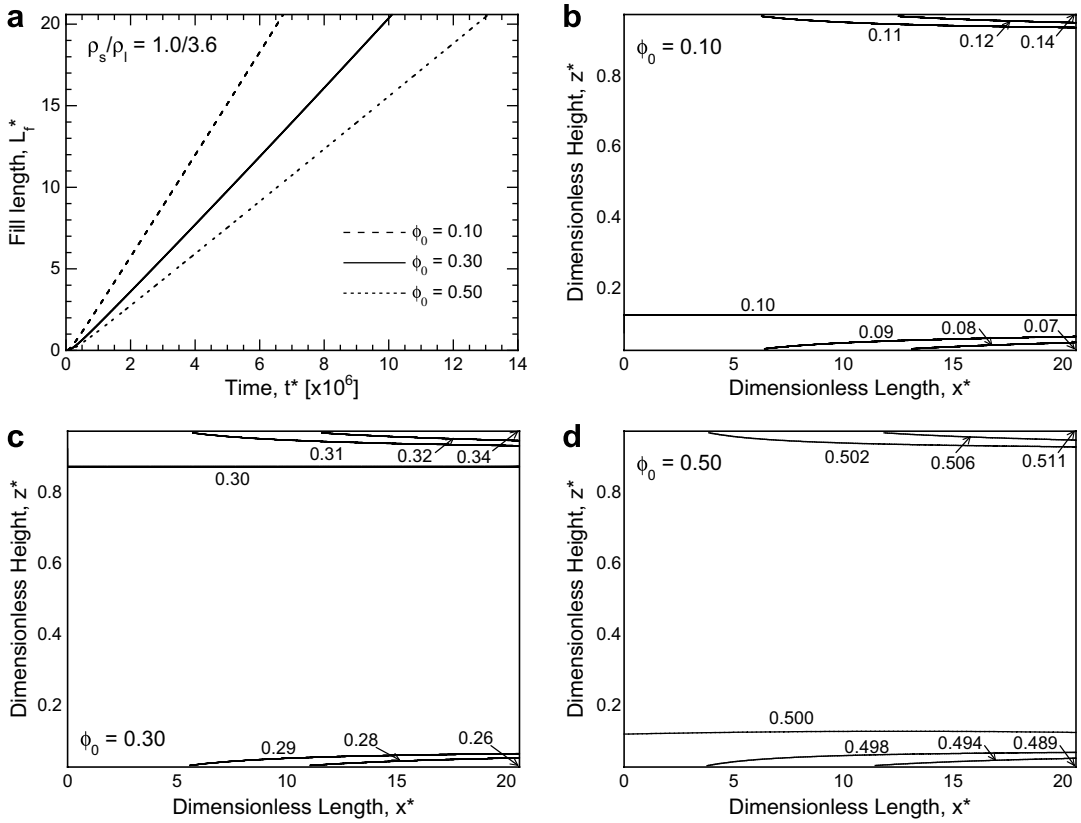

Fig. 6. (a) Effects of initial particle volume fraction ϕ_0 on the fill time; and the corresponding particulate volume fraction distributions for the initial volume fraction of (b) 0.10, (c) 0.29, and (d) 0.47, for floating case where $\rho_s/\rho_l = 1.0/3.6$.

cussion on the effects of the Ohnesorge number and the aspect ratio of the flow channel on the flow and settling characteristics will be presented only for the sinking case ($\rho_s/\rho_l = 3.6$).

Fig. 7 presents the fill times and the particle distributions for three different Ohnesorge numbers for the sinking case ($\rho_s/\rho_l = 3.6$), while other dimensionless parameters are fixed at $\phi_0 = 0.30$, $U_t^* = -5 \times 10^{-9}$ and $\gamma = 0.33$. Fig. 7a shows the evolution of fill length for the values of Ohnesorge number of 10, 20, and 40. For any given fill length, it is seen that the fill time increases as the Ohnesorge number Oh increases. Since the Ohnesorge number is defined as the ratio of viscous force to the surface tension, an increase in Ohnesorge number corresponds to a decrease in surface tension driving the flow or an increase in the viscous force; in either case, the capillary flow is retarded, thus increasing the fill time. Fig. 7b–d present the corresponding contours of particle volume fraction in the slurry at the time when the channel of length $L^* = 20.6$ is filled. As the Ohnesorge number increases, the nanoparticle distribution is seen to get progressively inhomogeneous. For the Ohnesorge number of $Oh = 10$ (Fig. 7b), the local particle volume fraction ranges from about 0.289 at the top right corner to about 0.311 at the bottom right corner, reflecting a nearly homogeneous dispersion as in the initial slurry in the reservoir. However, this range is seen to be about 0.25–0.34 for $Oh = 20$ (Fig. 7c) and 0.09–0.44 for $Oh = 40$ (Fig. 7d). For Ohnesorge number of 40, the large viscous effect (or equivalently, a reduced capillary driving force) and the corresponding decrease in the fill rate, provide sufficient fill time for most of the particles to settle, and a near separation of the particles and the liquid is observed in Fig. 7d, toward the end of the channel ($x^* = L_f^* = 20.6$).

The effects of the dimensions of the rectangular microchannel in terms of the aspect ratio γ, on the flow characteristics and settling of particles are presented in Fig. 8, by considering aspect ratios of: 0.33, 0.67 1.00, 1.50, and 3.00. For any specified fill length L_f, the fill time increases with the aspect ratio, as shown in Fig. 8a, due to the enhanced viscous effect resulting from the increased area of the microchannel walls; this results in a lower average flow velocity $\frac{dL_f}{dt}$. The contours of the particulate volume fraction inside the channel are presented in Fig. 8b–d, where it is seen that the maximum volume fraction ϕ at the bottom right corner of the channel increases with increasing aspect ratio, while ϕ at the top of the flow decreases.

The parametric studies presented above establish the effects of the flow characteristics, slurry properties, and channel dimensions on the particle distribution and fill time. Further, the results can be used to devise design windows identifying the range of the dimensionless parameters

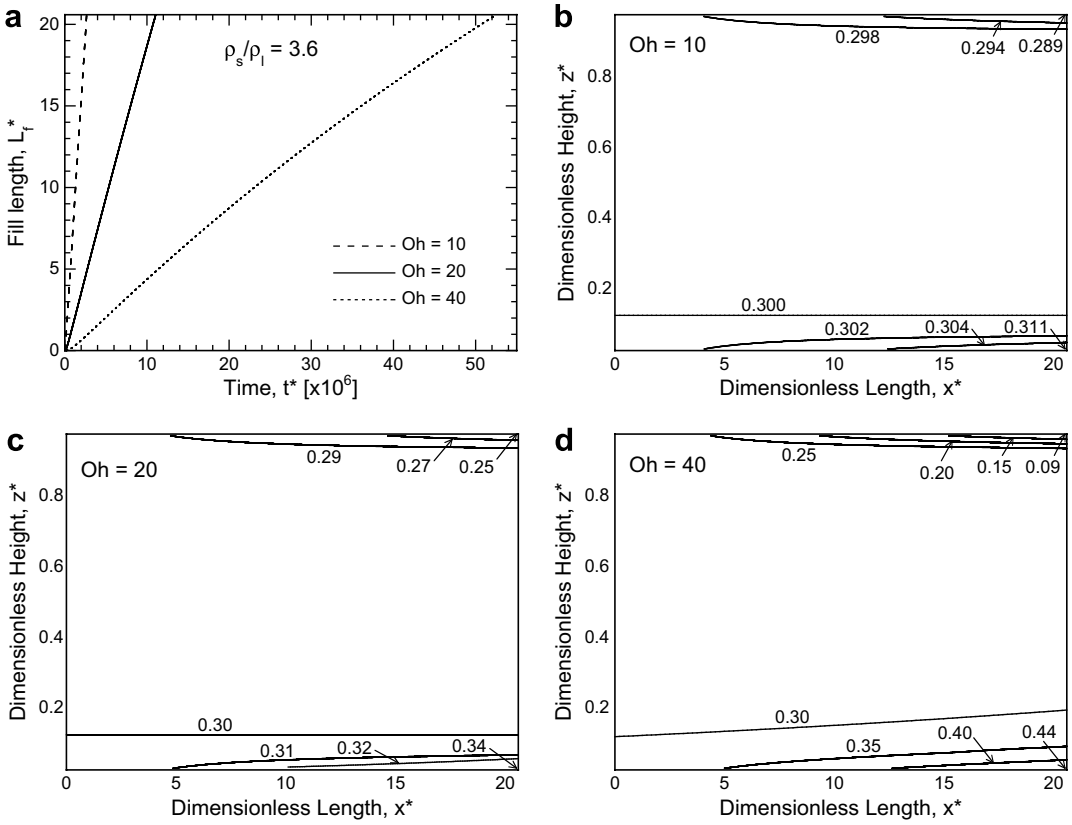

Fig. 7. (a) Effects of Ohnesorge number *Oh* on the fill time of slurry flow; and the corresponding particulate volume fraction distributions for the Ohnesorge number of (b) 15.64, (c) 31.28, and (d) 62.56, for sinking case where $\rho_s/\rho_l = 3.6$.

corresponding to a desired degree of homogeneity in the particle distribution at the end of the mold fill. For the microcasting process, a uniform particle distribution is desired to control shape deformation during the later sintering stage. To this end, a measure of homogeneity, Δ, is defined as the root-mean-square of a normalized local volume fraction deviation from the initial homogeneous particle volume fraction:

$$\Delta = \sqrt{\frac{1}{N_x N_z}\sum_{i=1}^{N_x}\sum_{j=1}^{N_z}\left(\frac{\phi_{i,j}-\phi_0}{\phi_0}\right)^2} \tag{18}$$

where $\phi_{i,j}$ is the local particle volume fraction at specific location, (x,z), N_x is the number of discrete x-locations in the computations, and N_z is total number of meshes in the z-direction. In this study, N_x is determined by the number of time steps used in solving Eq. (11) since $\phi(x,z)$ is related to $\phi(t,z)$ as per Eq. (17), and N_z is chosen to be 20 according to the mesh size used in the numerical model.

Numerical simulations are performed over various sets of nondimensional groups to analyze the effects of normalized Stokes velocity U_t^*, Ohnesorge number *Oh*, and aspect ratio γ on the inhomogeneity of particle distribution Δ. Fig. 9a shows the variation of particle distribution as a function of normalized Stokes velocity, for different initial particle volume fractions, while fixing other nondimensional groups ($Oh = 20$, $\gamma = 0.33$). It is seen that the inhomogeneity in the particle distribution, Δ, increases with the magnitude of normalized Stokes velocity and decreases with initial particle volume fraction. If the inhomogeneity of particle distribution is to be limited to a specified value, for example, 0.05 or 5% in this study, Fig. 9a indicates that for each initial particle volume fraction, there exists a maximum absolute value of normalized Stokes velocity $|U^*_{t,max}|$ below which the desired homogeneity is realized. These maximum allowable values of the normalized Stokes velocity are indicated by the vertical lines in Fig. 9a for various values of initial volume fraction. It should be noted that for $\phi_0 = 0.50$, for the range of normalized Stokes velocity considered, the homogeneity is always within the limit above. Following the presentation format in Fig. 9a, the effects of Ohnesorge number, *Oh*, and channel aspect ratio, γ, on the variation of particle distribution, Δ, for different initial particle volume fractions are presented in Fig. 9c and Fig. 9e, respectively. The solid lines in the figures correspond to the sinking case ($\rho_s/\rho_l = 3.6$), while the dashed lines correspond to the floating case ($\rho_s/\rho_l = 1.0/3.6$). For a fixed initial particle volume fraction, ϕ_0, the variation of particle distribution, Δ, increases with both the Ohnesorge number (Fig. 9c) and the aspect ratio (Fig. 9e), and the upper bound values of *Oh* and γ for a given ϕ_0 are identified in Fig. 9c and e by the vertical lines. It is seen that for $\phi_0 = 0.50$, all values of *Oh* and γ within the range studied

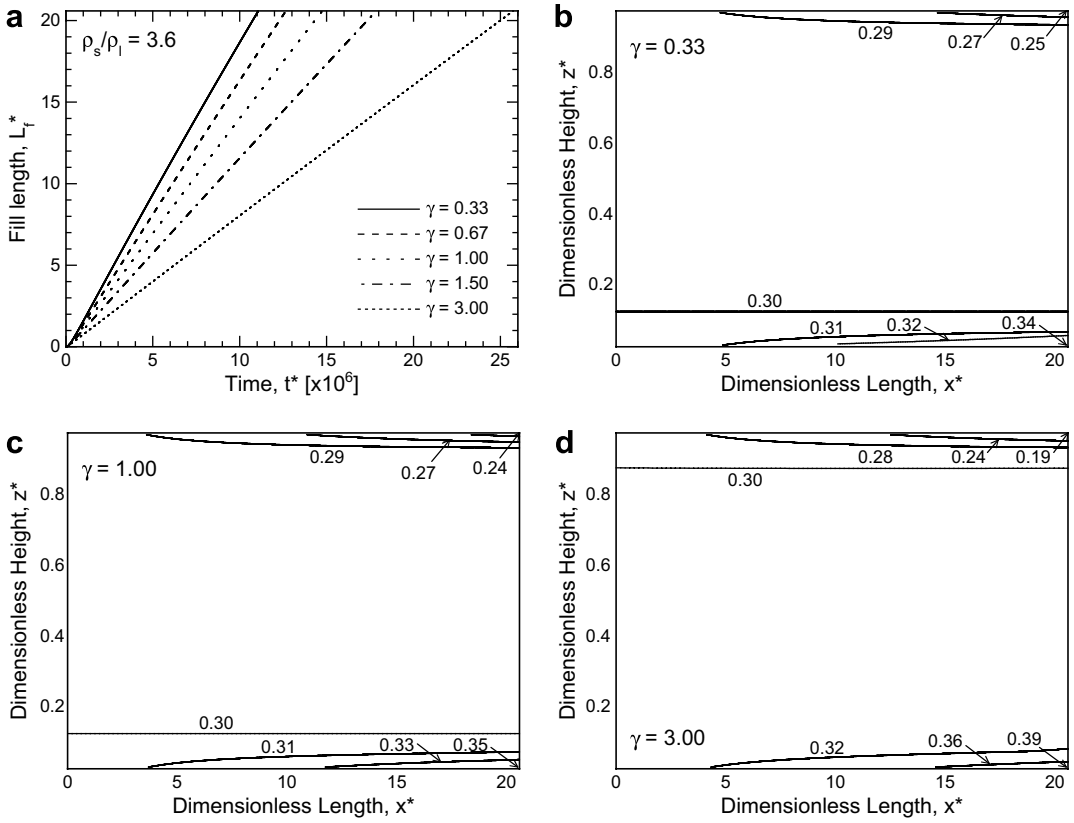

Fig. 8. (a) Effects of aspect ratio $\gamma = H/W$ on the fill time of slurry flow; and the corresponding particulate volume fraction distributions for the aspect ratio of (b) 0.10, (c) 0.33, and (d) 1.0, for sinking case where $\rho_s/\rho_l = 3.6$.

result in $\Delta \leqslant 0.05$, whereas for $\phi_0 = 0.10$ and 0.50, finite upper bounds are obtained.

From the results shown in Fig. 9a, c, and e, design windows which show the combinations of initial particle volume fraction and various nondimensional groups that result in the particle distribution homogeneity of less than a given value (0.05 in the current example) can be constructed. The design windows corresponding to the normalized Stokes velocity, U_t^*, Ohnesorge number, Oh, and aspect ratio, γ, are presented in Fig. 9b, d, and f, respectively, where the solid lines represent the particulate distributions with a variation $\Delta = 0.05$ for the sinking case, and the shaded areas identify the regions where $\Delta \leqslant 0.05$. The dashed lines in Fig. 9d and f represent the distribution with $\Delta = 0.05$ for the floating case. Fig. 9b shows that for small initial particle volume fraction, ϕ_0, which represents dilute slurries, there is greater potential for settling owing to the increased spacing between particles, and, therefore, the Stokes velocity has to be smaller to ensure homogeneity. As a design example, if an initial volume fraction, $\phi_0 = 0.20$, is given, for a fixed Ohnesorge number and aspect ratio, the maximum magnitude of normalized Stokes velocity $|U^*_{t,max}|$ resulting in $\Delta = 0.05$ is seen to be 5×10^{-9}, as indicated by point A in Fig. 9b, and smaller magnitude of normalized Stokes velocity approaching zero, as indicated by the shaded region, will lead to a more uniform particle distribution.

The design window identifying the combinations of the values of the Ohnesorge number, Oh, and the initial particle volume fraction, ϕ_0, corresponding to $\Delta \leqslant 0.05$, while other nondimensional groups are fixed, is shown in Fig. 9d as the shaded area. The solid line represents the combination of the values of Oh and ϕ_0 corresponding to $\Delta \leqslant 0.05$ for the sinking case ($\rho_s/\rho_l = 3.6$), while the dashed line represent that of the floating case ($\rho_s/\rho_l = 1.0/3.6$). To reduce the deviation, Δ, the maximum Ohnesorge number, Oh_{max}, has to decrease for a given initial volume fraction ϕ_0, and as ϕ_0 increases, the maximum Ohnesorge number that maintains the desired level of inhomogeneity also increases i.e., $Oh_{max} = 17$ for $\phi_0 = 0.1$ while $Oh_{max} = 35$ for $\phi_0 = 0.40$ for the sinking case, or $Oh_{max} = 17$ for $\phi_0 = 0.1$ while $Oh_{max} = 40$ for $\phi_0 = 0.40$ for the floating case. It is observed that, for large ϕ_0, slurries with floating particles allows for a larger Oh_{max} to maintain the same level of homogeneity compared to slurries with sinking particles. Physically, a large Ohnesorge number corresponds to small surface tension force or large viscous force. As the Ohnesorge number increases for any fixed initial volume fraction, the fill time increases due to the increased viscous resistance relative to the driving capillary force, which, in turn, provides sufficient time for the particles to settle, causing more inhomogeneity in the particle volume fraction distribution. As a design example, the critical point B ($Oh_{max} = 25$) in Fig. 9d signifies the maximum

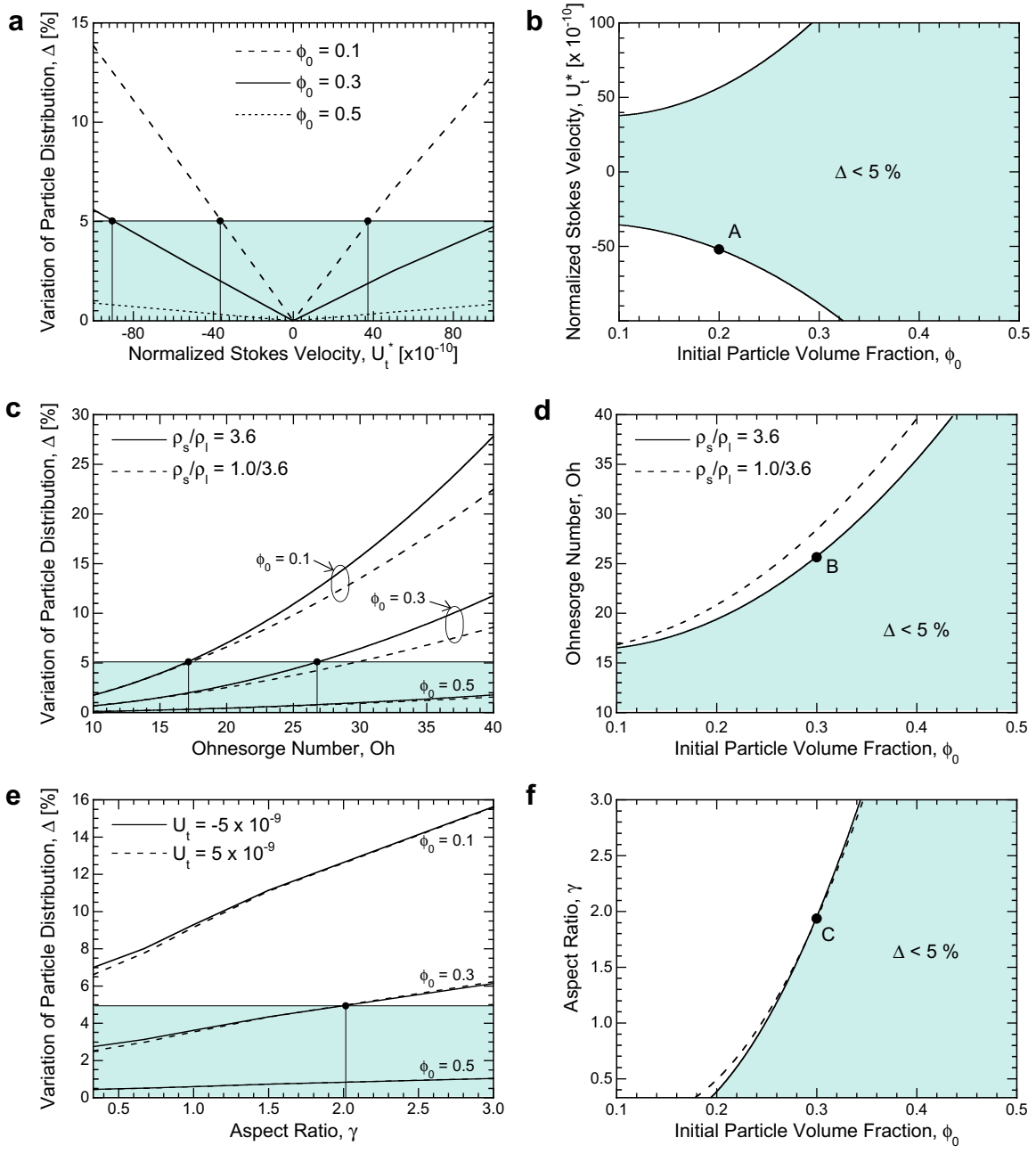

Fig. 9. Effects of initial particle volume fraction ϕ_0 and (a) normalized Stokes velocity U_t^*, (b) Ohnesorge number Oh, and (c) aspect ratio γ on the variation of particle distribution Δ; Design windows showing combinations of initial particulate volume fraction ϕ_0 and (d) normalized Stokes velocity U_t^*, (e) Ohnesorge number Oh, and (f) aspect ratio γ that result in a variation of particle distribution $\Delta \leqslant 0.05$ and superposed contours of dimensionless fill time.

Ohnesorge number that satisfies the particle distribution homogeneity constraint of $\Delta \leqslant 0.05$, for the initial particle volume fraction of $\phi_0 = 0.30$. In reality, the value of Ohnesorge number is bounded by the properties of the slurry used in the process, and therefore, the optimal design can be determined based on the available choice of materials and additives such as surfactants and dispersants that yield the smallest Ohnesorge number.

The design window on the maximum aspect ratio γ_{max} so as to achieve $\Delta \leqslant 0.05$ is presented in Fig. 9f, where it is seen that for large initial particle volume fraction, $\phi_0 > 0.34$, all values of the aspect ratio considered result in a particle distribution homogeneity of $\Delta \leqslant 0.05$. The maximum allowable aspect ratio corresponding to $\Delta \leqslant 0.05$ increases as ϕ_0 increases. As the initial particle volume fraction decreases from 0.34, the upper bound of aspect ratio decreases, and at $\phi_0 = 0.19$ the upper bound value decreases to $\gamma = 0.33$. Physically, a reduction in the aspect ratio reduces the viscous effect, shortens the fill time, and thus maintains the homogeneity of particle distribu-

tion. In the fabrication of high aspect ratio microstructures, Fig. 9f serves as a design plot to determine the maximum feasible aspect ratio for a given slurry design and material properties, so as to maintain a desired homogeneity. For example, the maximum aspect ratio for a 0.30 volume fraction slurry is seen to be 1.8 (Point C).

The parametric studies presented in this section illustrate the slurry flow characteristics with the simultaneous consideration of settling of the nanoparticulate solids during the mold-filling stage of a microcasting process. The design windows further summarize the ranges of nondimensional groups which result in homogeneous particle distribution. Further homogeneity may be obtained through the use of dispersants and other additives, as is typical in slurry formulation. The effects of these additional components on the settling behavior need to be considered in a future study. Further, the validated theoretical model and the design endeavor presented in this study provide for a basis for future development and optimization of the slurry composition as well as the microchannel design so as to obtain a tailored porosity distribution as required for the sintering stage of the process. Slurries with high concentration of nanoparticles are desired to achieve a dense product with minimal dimensional shrinkage; however, the increased viscosity associated with the higher particle loading translates to longer fill time. A trade-off between these competing considerations calls for a comprehensive theoretical modeling of the micromold filling and the nanoparticulate sintering steps of the process, which will be considered in a future study.

It should be noted that the present model does not account for the effects of Brownian motion on the flow and settling characteristics of the slurry, as the minimum corresponding Péclet (Pe) number for the cases considered in this study is about $Pe = 180$, which is relatively larger than $Pe = 10$, a regime where it is considered that the Brownian motion balances the hydrodynamic forces (Phung et al., 1996). A model which incorporates the Brownian motion may be considered for future work, from which a comparison to the present results may be conducted to determine the limiting particle size where the effects of Brownian motion may or may not be consequential.

4. Conclusions

A theoretical model was presented for the capillary-driven flow in a rectangular microchannel during a microcasting process. A systematic parametric investigation was conducted to explore the effects of four nondimensional groups representing a wide range of slurry compositions and flow parameters. The results showed that the fill time increases as the distribution of the particle volume fraction becomes inhomogeneous due to particle settling. The spatial gradient in the concentration of the particulate solid results in the viscosity gradient across the flow, which decreases the average flow velocity. Further, the settling characteristics, in terms of the particulate volume fraction distribution, are mainly dependent on the particle settling velocity, or the Stokes velocity. From the parametric studies, the effects of normalized Stokes velocity were found to be the most dominant on both flow and settling characteristics. The initial volume fraction distribution, the Ohnesorge number, and aspect ratio were additionally shown to affect the flow and settling characteristics. Design windows for the nondimensional groups were presented to identify the upper bounds of the normalized Stokes velocity, Ohnesorge number, and aspect ratio, as a function of initial particle volume fraction. The regions bounded below the upper limits correspond to conditions which yield the variation of particle distribution to be near homogeneous. The paper represents an early theoretical work in the modeling and optimization of the particle distribution of nanoparticulate slurry during microcasting. Additional considerations, including design using the molecular modeling of the suspension with dispersants or surfactants, will be reported in a future work.

Acknowledgemenst

The work reported is funded by the National Science Foundation through Grant No. CTS-0522933. The authors gratefully acknowledge the support.

References

Allan, S.M., Chang, C.C., Shulman, H.S., Morales, A.M., 2003. Precision microgear fabrication and sintering with microwaves. In: Proceedings of the 27th International Cocoa Beach Conference on Advanced Ceramics and Composites: A CESP 24 (3).

Barraza, H.J., Kunapuli, S., O'Rear, E.A., 2002. Advancing contact angles of newtonian fluids during "high" velocity, transient, capillary-driven flow in a parallel plate geometry. J. Phys. Chem. B 106, 4979–4987.

Batchelor, G.K., 1982. Sedimentation in a dilute polydisperse system of interacting spheres. Part 1. General theory. J. Fluid. Mech. 119, 379–408.

Batchelor, G.K., Wen, C.S., 1982. Sedimentation in a dilute polydisperse system of interacting spheres. Part 2. Numerical results. J. Fluid. Mech. 124, 495–528.

Berezkin, V.V., Churaev, N.V., 1982. Changes in contact angle during the process of capillary rise. Colloid J. USSR 44, 376–382.

Brittin, W.E., 1946. Liquid rise in a capillary tube. J. Appl. Phys. 17, 37–44.

Bürger, R., Concha, F., 1998. Mathematical model and numerical simulation of the settling of flocculated suspensions. Int. J. Multiphase Flow 24, 1005–1023.

Bürger, R., Fjelde, K.K., Hofler, K., Hvistendahl Karlsen, K., 2001. Central difference solutions of the kinematic model of settling of polydisperse suspensions and three-dimensional particle-scale simulations. J. Eng. Math. 41, 167–187.

Concha, F., Lee, C.H., Austin, L.G., 1992. Settling velocities of particulate systems: 8. Batch sedimentation of polydispersed suspensions of spheres. Int. J. Mineral Process. 35, 159–175.

Dreyer, M., Delgado, A., Rath, H.J., 1993. Fluid motion in capillary vanes under reduced gravity. Microgravity Sci. Technol. 4, 203–210.

Dreyer, M., Delgado, A., Rath, H.J., 1994. Capillary rise of liquid between parallel plates under microgravity. J. Colloid Interface Sci. 163, 158–168.

Duarte, A.A., Strier, D.E., Zanette, D.H., 1996. The rise of a liquid in a capillary tube revisited: a hydrodynamical approach. Am. J. Phys. 64, 413–418.

Garino, T.J., Morales, A., Buchheit, T., Boyce, B., 2002. The fabrication of stainless steel parts for MEMS. Mater. Res. Soc. Proc. 687, 149–154.

Garino, T.J., Cesarano, J., Morales, A., 2003. The development of alternative molds for micromolding. Mater. Res. Soc. Proc. 741, 227–232.

Garino, T.J., Morales, A., Boyce, B.L., 2004. The mechanical properties, dimensional tolerance and microstructural characterization of micromolded ceramic and metal components. Microsyst. Technol. 10, 506–509.

Gietzelt, T., Piotter, V., Ruprecht, R., Hausselt, J., 2002. Manufacturing of isolated ceramic microstructures. Microsyst. Technol. 9, 99–103.

Hamraoui, A., Thuresson, K., Nylander, T., Yaminsky, Y., 2000. Can a dynamic contact angle be understood in terms of a friction coefficient. J. Colloid Interface Sci. 226, 199–204.

Hamraoui, A., Nylander, T., 2002. Analytical approach for the Lucas–Washburn equation. J. Colloid Interface Sci. 250, 415–421.

Han, S., Wang, K.K., 1997. Analysis of flow of encapsulant during underfill encapsulation of flip-chips. IEEE Trans. Components, Packaging, Manuf. Technol. B 20, 424–433.

Hormes, J., Göttert, J., Lian, K., Desta, Y., Jian, L., 2003. Materials for LiGA and LiGA-based microsystems. Nucl. Instr. Methods Phys. Res. B 199, 332–341.

Krieger, I.M., Dougherty, T.J., 1959. A mechanism for the non-Newtonian flow in suspensions of rigid spheres. Trans. Soc. Rheol. 3, 137–152.

Kurganov, A., Tadmor, E., 2000. New high resolution central schemes for nonlinear conservation laws and convection–diffusion equations. J. Comp. Phys. 160, 241–282.

Kynch, G.J., 1952. A theory of sedimentation. Trans. Faraday Soc. 48, 166–176.

Levine, S., Reed, P., Watson, E.J., 1976. A theory of the rate of rise of a liquid in a capillary. In: Kerker, M. (Ed.), Adsorption, Catalysis, Solid Surfaces, Wetting, Surface Tension, and Water. In: Colloid and Interface Science, vol. III. Academic Press, New York, pp. 403–419.

Merz, L., Rath, S., Piotter, V., Ruprecht, R., Hausselt, J., 2004. Powder injection molding of metallic and ceramic microparts. Microsyst. Technol. 10, 202–204.

Morales, A.M., Zhang, Z.J., Chinn, D., 2001. Fabrication of Ceramic Microstructures from Polymer Compositions Containing Nanoparticles, United States Patent 6 245 849 B1.

Morales, A.M., Winter, M.R., Domeier, L.A., Allan, S.M., Skala, D.M., 2002. Fabrication of Metallic Microstructures by Micromolding Nanoparticles, United States Patent 6 472 459 B2.

Morales, A.M., Pitchumani, R., Garino, T.J., Gutmann, A.K., Domeier, L.A., 2005. Fabrication of ceramic microstructures via microcasting of nanoparticulate slurry. J. Am. Ceram. Soc. 88, 570–578.

Newman, S., 1968. Kinetics of wetting of surfaces by polymers; capillary flow. J. Colloid Interface Sci. 26, 209–213.

Phung, T.N., Brady, J.F., Bossis, G., 1996. Stokesian dynamics simulation of Brownian suspensions. J. Fluid. Mech. 313, 181–207.

Piotter, V., Mueller, K., Plewa, K., Ruprecht, R., Hausselt, J., 2002. Performance and simulation of thermoplastic micro injection molding. Microsyst. Technol. 8, 387–390.

Press, W.H., Flannery, B.P., Teukolsky, S.A., Vetterling, W.T., 1986. Numerical Recipes: The Art of Scientific Computing. Cambridge University Press, New York.

Schonhorn, H., Frisch, H., Kwei, T.K., 1966. Kinetics of wetting of surfaces by polymer melts. J. Appl. Phys. 37, 4967–4973.

Shannon, P.T., Tory, E.M., 1965. Settling of slurries. Ind. Eng. Chem. 57 (2), 18–25.

Soboleva, O.A., Bogdanova, Y.G., Summ, B.D., 2000. Specific features of the capillary rise of aqueous solutions of binary surfactant mixture. Colloid J. 62, 683–687.

Summ, D., Raud, E.A., 1991. Dependence of dynamic contact angles on the flow velocity. Heat. Transfer – Sov. Res. 23, 528–531.

Washburn, E.W., 1921. The dynamics of capillary flow. The Phys. Rev. 17 (3), 273–283.

Xiao, Y., Yang, F., Pitchumani, R., 2006. A generalized analysis of capillary flows in channels. J. Colloid Interface Sci. 298, 880–888.